Graphene-based tunable multi-band metamaterial polarization-insensitive absorber for terahertz applications

Prince Jain[1] · Shonak Bansal[1] · Krishna Prakash[1] · Neha Sardana[3] · Neena Gupta[1] · Sanjeev Kumar[2] · Arun K. Singh[1]

Abstract

This paper presents a graphene-based tunable polarization-insensitive metamaterial absorber (MMA) at terahertz (THz) frequencies. The absorber consists of top patterned gold (Au) layer followed by single layer of graphene, dielectric spacer, and Au layer at bottom. The proposed MMA demonstrates multi-band absorption with the characteristics of both broad- and dual-band absorption by optimizing dimensions (parametric analysis). Broad-band absorption reaches over 90% for the range of 4.57–6.45 THz with the relative absorption bandwidth of 34%, and the absorption peak at 6.86 and 7.20 THz having 98.9 and 95.2% absorption. The normalized impedance and constitutive electromagnetic parameters of the MMA are calculated using the Nicolson–Ross–Weir (NRW) method to validate the absorption rate. Furthermore, proposed absorber is polarization-insensitive upto 90° for transverse electric wave. The tunable characteristic of MMA is achieved by tuning the Fermi energy of graphene with the application of bias voltage. Accordingly, the proposed multi- and broad-band absorbers find its potential applications in spectroscopy detection, imaging, and sensing.

1 Introduction

Metamaterials are artificially engineered materials that exhibit exceptional electromagnetic (EM) properties including negative refractive index [1], perfect lensing [2], and cloaking [3]. Several devices such as switches [4], filters [5], modulators [6], antennas [7], and solar cells [8] have been demonstrated using the exotic properties of the metamaterials. The intrinsic losses in metamaterials degrade their performance at THz frequencies due to the metallic resonators. Such losses can be decreased either by employing the gain materials [9] or by optimizing the structural geometries [10]. However, absorption losses in the metamaterial can be used to design perfect metamaterial absorbers (MMAs).

The perfect MMA consisting of metallic split ring and cut-wire insulated with dielectric spacer was first introduced by Landy et al. [11]. The perfect absorbers have found their potential utilization in several applications including sensing [12, 13], solar cells [8], thermal emitter [14], and photodetectors [15]. The MMAs are also being proposed in the range of microwave to terahertz frequencies for dual-, [16–18], triple- [19], multi- [20], broad-band [21], tunable [12], and polarization-insensitive operations [16, 19]. Among these, multi- and broad-band absorbers have various applications including sensors, photodetectors and broad-band communication etc. There are two ways to increase the absorption peaks either by stacking of differently sized layers [21, 22], or incorporating different resonators into a unit cell [20, 23]. However, such methods are inappropriate for several realistic applications due to fabrication complexity at THz range. Some complicated configurations such as dual-, triple-, and quadruple-ring have been proposed to obtain dual- and triple-band MMAs [24–26]. Zhao et al. [27] demonstrated a switchable vanadium dioxide-based MMA with bandwidth of 1.2 THz. Further few works have been reported on the dual-band, tunable, and broad-band absorption [28–30]. Multi-band characteristics are typically being realized by utilizing different size metallic resonators or by stacking multiple layers of absorbers [31–33]. The multi-band absorption with simple design configurations has been demonstrated with polarization angle sensitivity in

✉ Arun K. Singh
  arun@pec.edu.in

[1] Department of Electronics and Communication Engineering, Punjab Engineering College (Deemed To Be University), Chandigarh, India

[2] Department of Applied Sciences, Punjab Engineering College (Deemed To Be University), Chandigarh, India

[3] Department of Metallurgical and Materials Engineering, IIT Ropar, Rupnagar, India

refs.[34–36]. In recent times, frequency tunable properties in MMAs was crucial for the practical applications [37]. Wang et al. [38] proposed a frequency tunable MMA by changing the position of metallic patch. Such designs are quite impractical with moving top layer on a fixed structure and are difficult to fabricate.

The extraordinary properties of graphene such as high optical transparency, conductivity, electron mobility, and flexibility make it suitable material for futuristic applications [39–41]. The Fermi energy (E_F), electric conductivity, and relative dielectric constant of graphene can be tuned by varying the bias voltage, which makes it a desirable material for developing frequency tunable MMAs [16, 17, 42–44]. These graphene-based MMAs provide a great opportunity for frequency tunable characteristics of the terahertz absorbers.

Despite previous studies on the development of MMAs having multi-and/or broad-band absorption characteristics, there is no single metallic structure-based MMA demonstrating dual characteristic, *i.e.*, multi- and broad-band absorption to the best of our knowledge. Hence, in this work, we have proposed a novel design of graphene-based multi-and broad-band MMA which comprises of split-circular ring connected diagonally to operate in the frequency range of 4 to 8 THz. The MMA exhibits average and maximum absorption of 98.24% and 99.4% (at resonating frequency of 6.34 THz), respectively, for transverse magnetic (TM) polarization. For transverse electric (TE) polarization, it demonstrates the average and maximum absorption of 96.6% and 99.7% (at resonating frequency of 5.6 THz), respectively. Moreover, the absorption bandwidth of the MMA can easily be tuned by changing the Fermi level of the graphene which is quite significant instead of changing the metallic patch position as proposed in ref. [38]. The normalized impedance and constitutive EM parameters are estimated using the Nicolson–Ross–Weir (NRW) method [45, 46] to validate the absorptivity. The proposed structure is further analyzed at different polarization and incident angles.

2 Design and simulation

The proposed MMA is simulated utilizing finite element method (FEM)-based ANSYS HFSS software applying periodic boundary conditions in both *x*- and *y*-direction and Floquet periodic port in the *z*-direction, so that the MMA can become an infinite periodic array. The electric and magnetic field components are incident on the unit cell as shown in the Fig. 1a. The proposed absorber comprises of Au/SiO$_2$/graphene/Au materials from the bottom to top as illustrated in Fig. 1a. The geometric parameters of the MMA are $a = 43.8$ μm, $b = 2$ μm, $d = 26$ μm, $w_1 = 2$ μm, $w_2 = 2.2$ μm, $w_3 = 2.4$ μm, $w_4 = 2.6$ μm, $g = 2.4$ μm. The thickness of gold is 0.2 and 0.3 μm at the top and bottom layers, respectively, with an electrical conductivity (σ) of 4.09×10^7 S/m. The thickness of SiO$_2$ layer is 8.1 μm with a relative permittivity (ε_r) of 3.9 [42, 47, 48]. The absorptivity ($A = 1 - |S_{11}|^2 - |S_{21}|^2$) of proposed MMA is estimated from the S-parameters, where S_{11} and S_{21} represent the reflection and transmission coefficients, respectively. The maximum absorption is obtained by minimizing both reflection and transmission. The transmission coefficient of the absorber is zero ($S_{21} = 0$) over the entire band by keeping the thickness of bottom gold plane larger than that of its skin depth as shown in Fig. 1b. To minimize the reflection coefficient and let the energy of the incident EM wave to be absorbed, the impedance of the absorber is adjusted so as to match the impedance in free space.

The complex permittivity of graphene is calculated by $\varepsilon_g = 1 + i\sigma_g/\omega\varepsilon_0\Delta$ [47], where $\varepsilon_0 = 8.854 \times 10^{-12}$ F/m is the vacuum permittivity, Δ is the single-layer graphene thickness
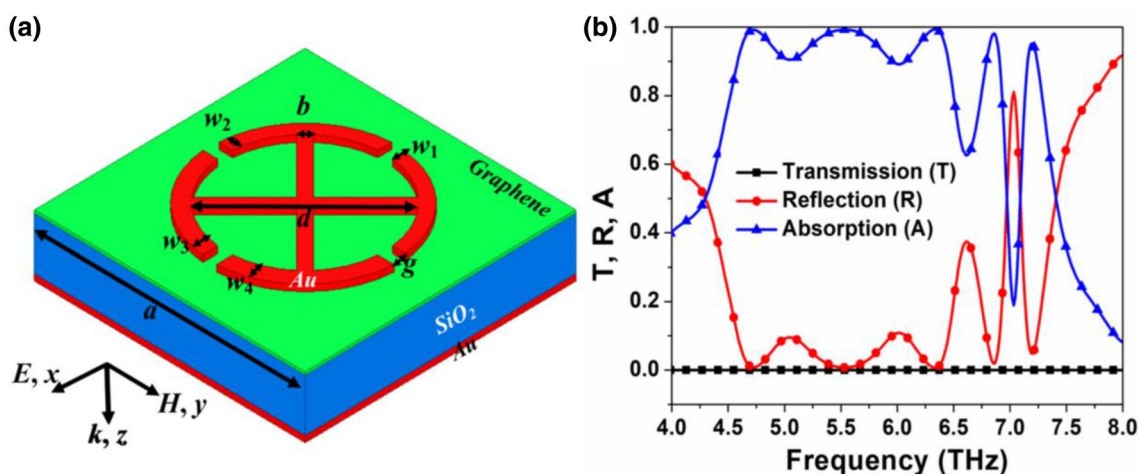

Fig. 1 Proposed metamaterial absorber (MMA). **a** Schematic view. **b** Transmission, reflection, and absorption spectra

(0.5 nm) and σ_g is graphene conductivity estimated by the Kubo formula [48]. The permittivity can be tuned with change in E_F, which makes graphene a suitable material for tunable absorbers. The calculated permittivity is further integrated in the computer simulations to analyze the influence of graphene on the MMA.

3 Results and Discussions

The proposed MMA demonstrates both multi- and broadband absorption from 4 to 8 THz, as shown in Fig. 1b. The absorption bandwidth is more than 90% for 4.57–6.45 THz (i.e., broad-band spectra) with the relative absorption bandwidth (RAB) of 34% and is superior to previously reported broad-band absorption device [49]. The absorption performance, i.e., $RAB = 2(f_H - f_L)/(f_H + f_L)$, where f_H and f_L represent the higher and lower frequency, respectively, with absorption above 90%. The absorptivity at resonating frequencies of 4.73, 5.55, 6.34, 6.86, and 7.20 THz are 99.3, 99.2, 99.4, 98.1, and 95.2%, respectively, for TM polarization. It is further observed that there is no obvious difference between TE and TM polarized wave due to almost symmetric shape of the MMA as shown in Fig. 2. For TE polarization, absorptivity of 99.6, 99.7, 99, 94.7, and 90% is achieved at resonating frequencies of 4.64, 5.6, 6.33, 6.77, and 7.18 THz, respectively. For TM and TE polarization, the average absorption is 98.24 and 96.6%, respectively. Thus, the structure is polarization insensitive. Figure 3 illustrates the absorption performance with the E_F of graphene varying from 0.2 to 0.8 eV. It is observed that the absorption peak position can be altered easily by varying E_F, e.g., increase in E_F, decreases the real part of the permittivity which further tunes the properties of graphene [43, 50, 51].
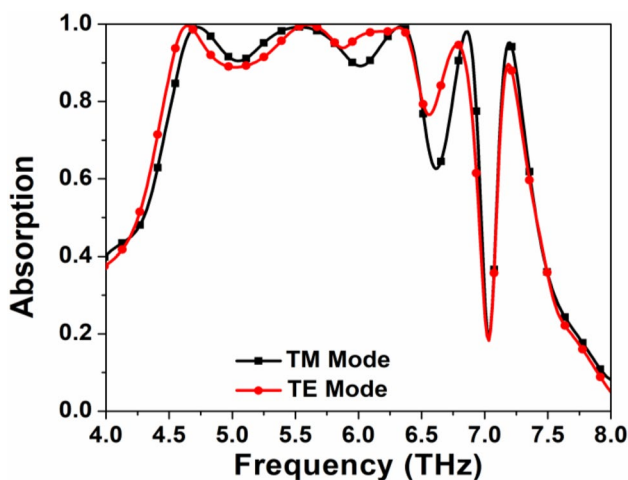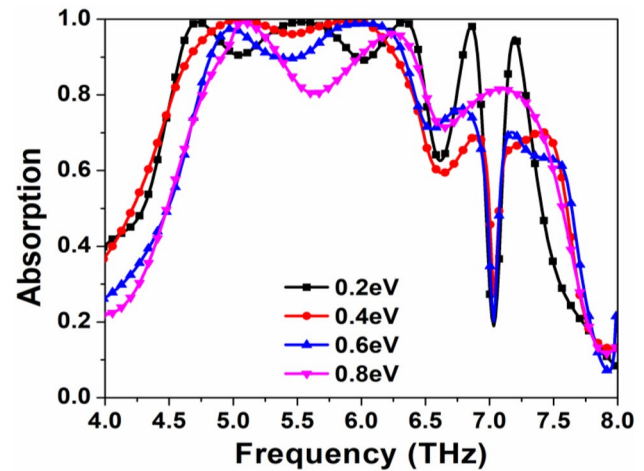
Fig. 3 Absorption peaks with different Fermi energy

The absorbance mechanism is validated by the normalized impedance of the proposed MMA, and is estimated by [17, 19]

$$Z = \sqrt{\frac{\left(1 + S_{11}\right)^2 - S_{21}^2}{\left(1 - S_{11}\right)^2 - S_{21}^2}} = \frac{1 + S_{11}}{1 - S_{11}} \left(\text{for } S_{21} = 0\right) \quad (1)$$

In order to obtain better absorption, the free space impedance must be equal to MMA impedance; hence, real and imaginary impedance should be nearly one and zero, respectively. This ensures zero reflectance and maximum absorption at those frequencies. The normalized impedance of $1.17 + j0.08$, $1.19 + j0.002$, $0.86 + j0.06$, $1.14 - j0.26$, and $0.81 - j0.35$ are found at 4.73, 5.55, 6.34, 6.86, and 7.20 THz, respectively, as demonstrated in
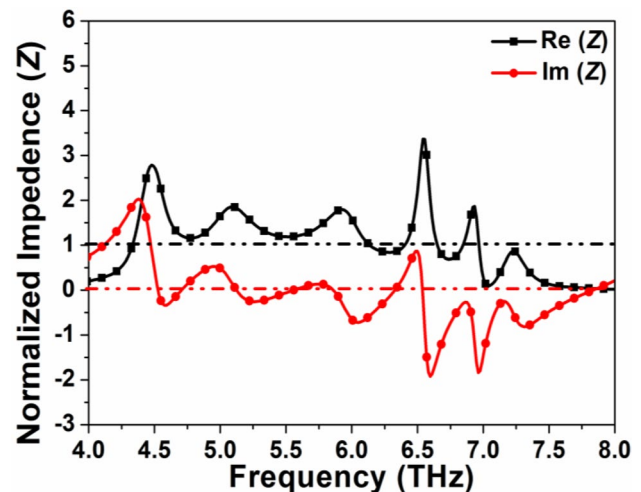
Fig. 2 Absorption peaks for TM and TE polarization

Fig. 4 Normalized impedance of the MMA

Fig. 4. It is noted that the first three peaks have better impedance matching as compared to the last two peaks. The absorption peak is slightly less at 7.20 THz due to the high reactance. Table 1 shows the real, imaginary, and absolute values of normalized impedance and constitutive EM parameters for every resonating frequency.

The constitutive EM parameters, i.e., effective permittivity (ε_{eff}) and effective permeability (μ_{eff}) of the absorber are calculated by employing the NRW method [45, 46]. In order to achieve perfect absorption, ε_{eff} must be equal to μ_{eff}, as $Z = \sqrt{\mu_{eff}/\varepsilon_{eff}}$, resulting in unity impedance. The frequency response of ε_{eff} and μ_{eff} for the proposed MMA is illustrated in Fig. 5. Table 1 concludes that the real and imaginary parts of the EM parameters are almost same at all absorption peaks except at 7.20 THz, which again validate the lower absorption.

Parametric analysis with the structure parameters is carried out to realize the absorption spectra. The obtained absorption spectra by employing parametric analysis are illustrated in Figs. 6 and 7. The effect of variation in dielectric spacer thickness from 7.1 to 9.1 µm is studied on absorption performance while keeping other structure parameters constant. It is clear from Fig. 6 that with increase in thickness, the absorption frequencies exhibit red shift phenomenon, which can be estimated by transmission phase [52, 53]:

$$\alpha = \frac{4h\sqrt{\varepsilon_r - \sin^2\theta}}{\lambda} \qquad (2)$$

where h is the dielectric spacer thickness, ε_r is the dielectric constant, θ and λ are the incident angle and wavelength, respectively. With constant value of ε_r, θ, and α, the ratio h/λ is remain fixed. Accordingly, the substrate thickness is inversely proportional to the resonating frequency. Therefore, resonating frequencies shift to lower frequency with the increase in dielectric spacer thickness. As a result, best absorption peaks are found at dielectric spacer thickness of 8.1 µm. Moreover, we can clearly see in Fig. 6b that as the dielectric spacer thickness is increasing from 7.1 to 9.1 µm, the resonating frequencies are red shifted (moving towards lower frequencies).
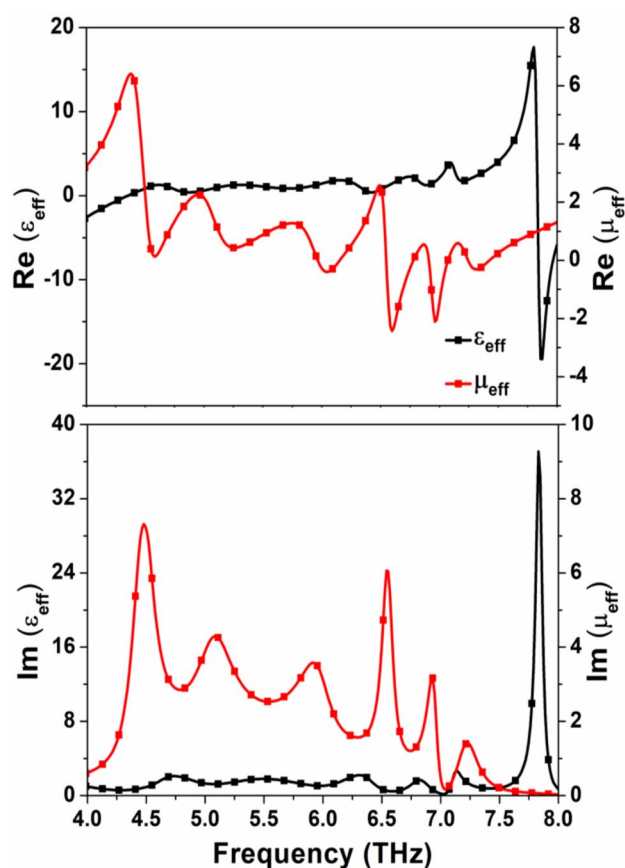

Fig. 5 Constitutive electromagnetic parameters of MMA

Figure 7a and b demonstrates that with the increase in the unit cell dimensions (*a*), the absorption peaks shift towards the lower frequencies. This is due to the relation between unit cell dimensions and wavelength which are directly proportional to each other. The transmission, reflection, and absorption spectra without ground plane are illustrated in Fig. 8 with less than 40% absorption for whole spectrum which shows the role of bottom metallic plane when compare to Fig. 1b.

The performance of the MMA at different polarization angles varying from 0° to 90° is illustrated in Fig. 9a. According to the results, the absorption is almost insensitive

| Table 1 Comparison of normalized impedance and constitutive electromagnetic parameters of the proposed MMA	Frequency (THz)	Absorption rate (%)	Re (Z)	Im (Z)	|Z|	Re (ε_{eff})	Im (ε_{eff})	|ε_{eff}|	Re (μ_{eff})	Im (μ_{eff})	|μ_{eff}|
	4.73	99.3	1.17	0.08	1.17	1.00	2.09	2.31	0.99	2.98	3.14
	5.55	99.2	1.19	0.002	1.19	0.99	1.77	2.02	1.00	2.53	2.72
	6.34	99.4	0.86	0.06	0.86	0.97	2.13	2.34	1.02	1.61	1.90
	6.86	98.1	1.14	− 0.26	1.16	1.33	1.42	1.94	0.54	1.97	2.04
	7.20	95.2	0.81	− 0.35	0.88	1.75	1.69	2.43	0.41	1.33	1.39
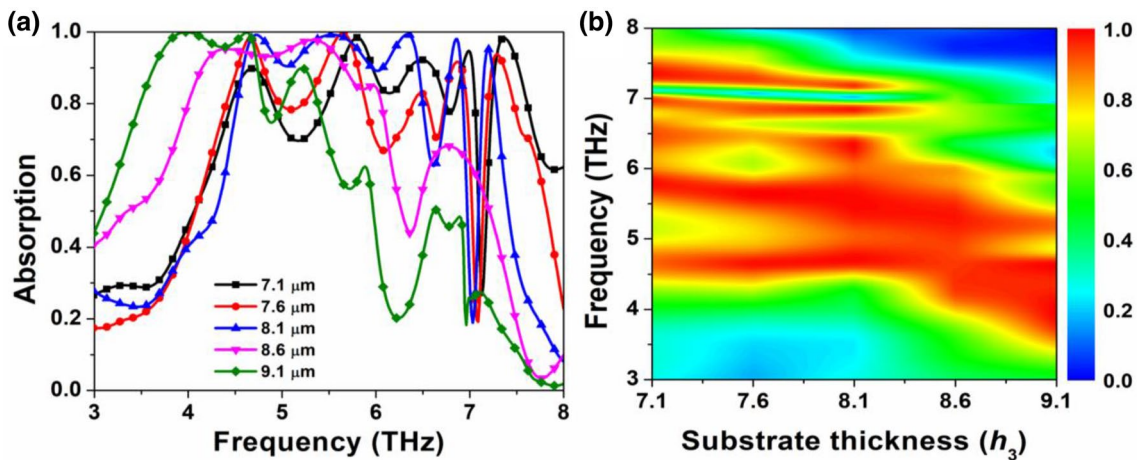
Fig. 6 Absorption spectra with the change in dielectric spacer thickness from 7.1 to 9.1 µm are shown in **a** and **b**
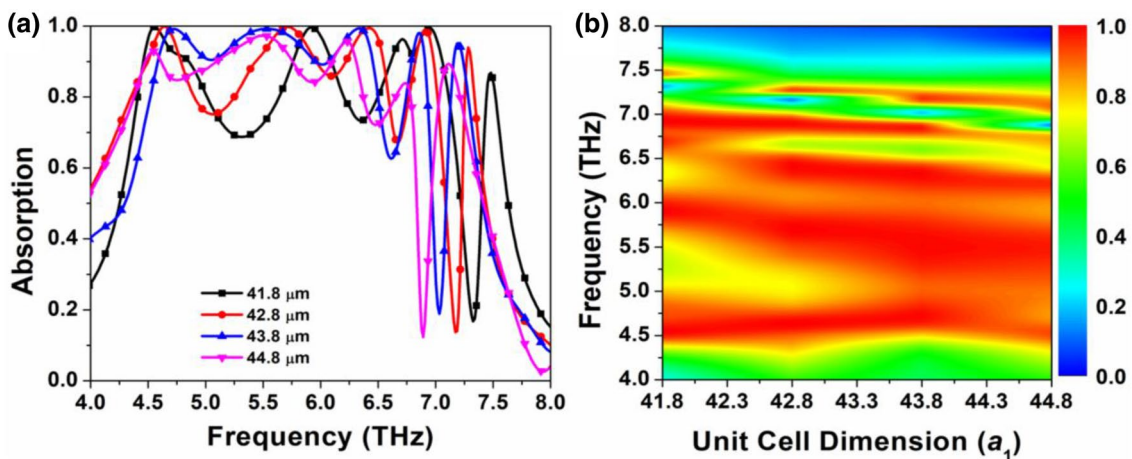

Fig. 7 Absorption spectra with the change in unit cell dimensions from 41.8 to 44.8 µm are shown in **a** and **b**
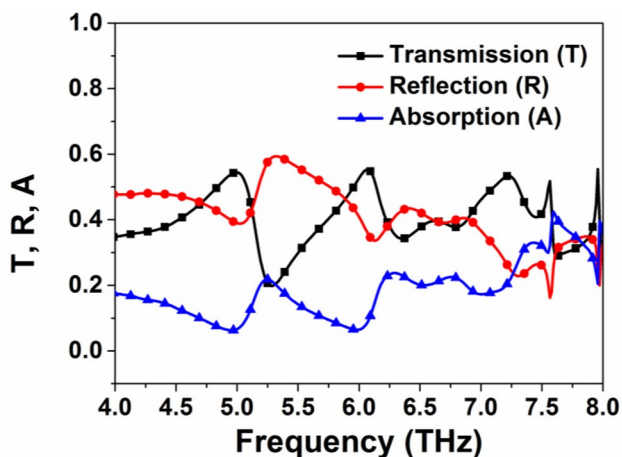

Fig. 8 Transmission, reflection, and absorption spectra without ground plane

of polarization angle due to almost symmetrical shape of structure. Such characteristics can be utilized for THz sensing, detection, and optoelectronic applications. The absorption spectra with different incident angles varying from 0° to 45° are illustrated in Fig. 9b. As the angle increases, the absorption will decrease because reflection of light is increased at higher incidence angles. The magnetic dipole oscillation of the MMA is efficiently excited with the increase in incident angle to achieve better absorption at other resonating frequencies similar to other previous studies [28, 34, 52]. The design offers more than 90% absorption with an incidence angle of 45° for quad-band absorption.

Figure 10 shows the electric field and surface current distribution for normal incidence of proposed MMA to observe the absorption at 4.73, 5.55, 6.34, 6.86, and 7.20 THz. The results suggest that the electric field mainly distributes on the edges of split rings and wires that means resonance is
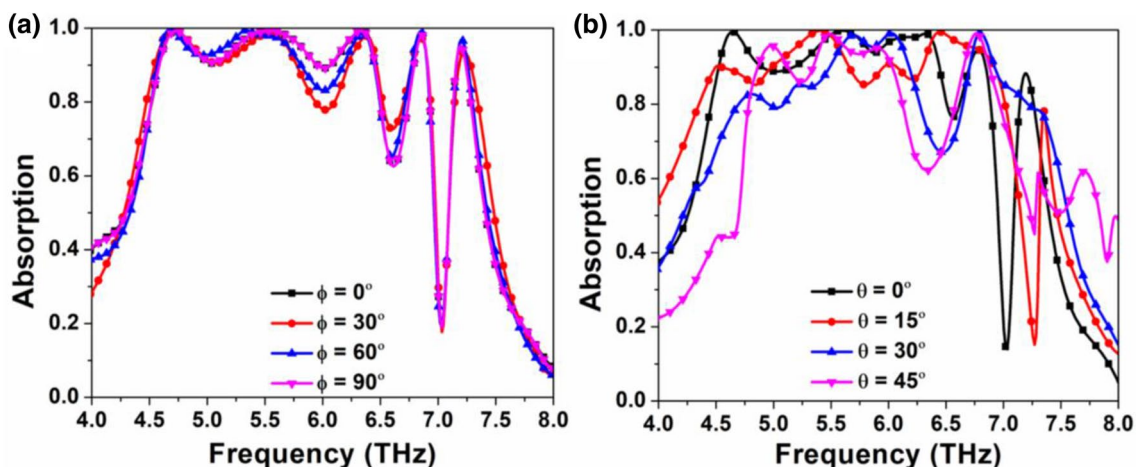
Fig. 9 Absorption of the proposed MMA. **a** with various polarization angles. **b** with various incident angles
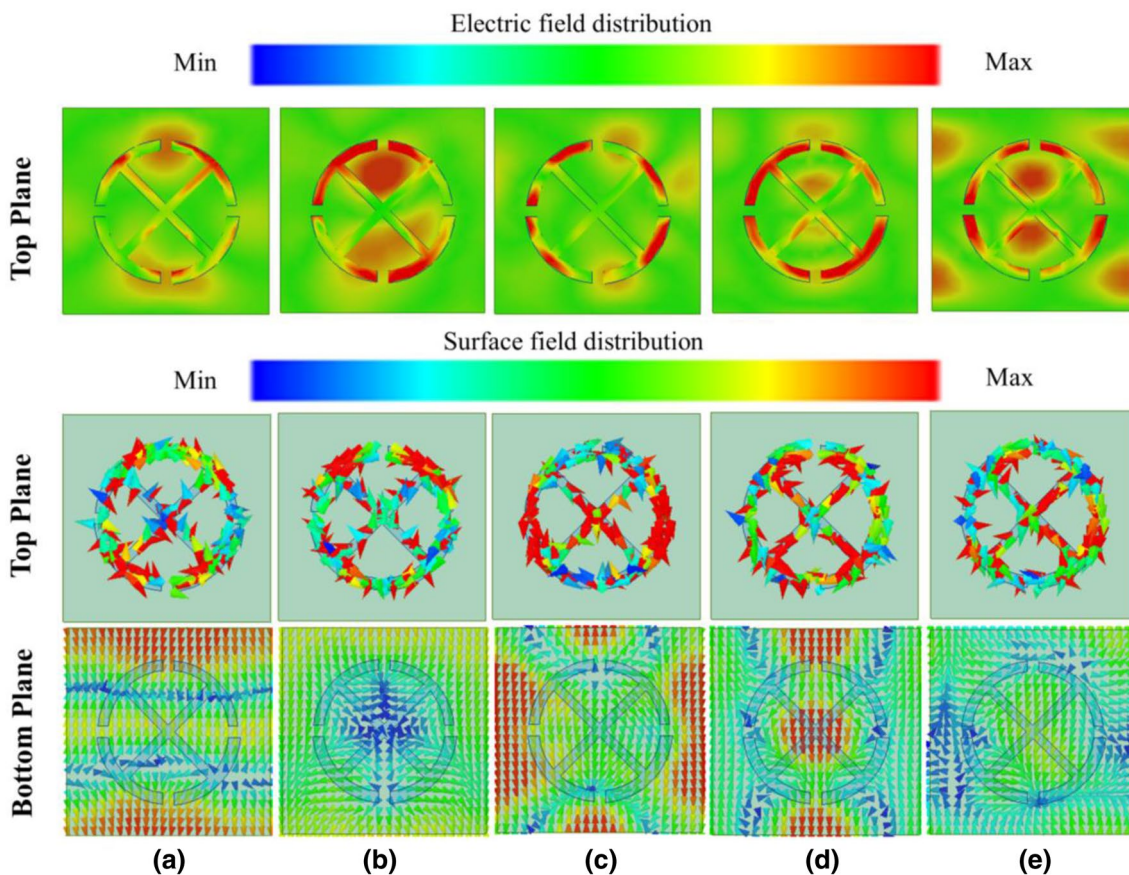

Fig. 10 Electric field distribution on the top layer and surface current distribution on the top and bottom layer. **a** 4.73 THz. **b** 5.55 THz. **c** 6.34 THz. **d** 6.86 THz. **e** 7.20 THz

mainly concentrated at some parts of the metal at lower frequencies, whereas at higher frequencies, it is more localized at some parts of graphene and metal due to the higher order of resonance. Figure 10 clearly depicts that the current distribution on the bottom metallic layer mainly flow in the opposite direction than that of top metallic layer. The strong magnetic resonance is exhibited because of the current loop formed by the anti-parallel surface currents. Such excitation

of the magnetic and electric resonances results in the five absorption peaks.

Table 2 presents the comparison of our proposed MMA with the previously reported multi-band MMAs on the basis of absorption peaks, absorptivity, and polarization suggesting that the proposed tunable MMA exhibits five absorption peaks with high absorptivity, *i.e.*, 95.2–99.4% and 90–99.7% for TM and TE Mode, respectively, and polarization-insensitive characteristics utilizing only a single metallic structure. However, previously reported MMAs have achieved multi-band characteristics by incorporating multiple metallic resonators of different size [54, 55, 57–59] in a single unit cell. In ref.[56], a quad-band absorber having single metallic structure demonstrates lower absorption rate between 75 and 95% with polarization sensitive characteristics. On the other hand, Table 3 demonstrates the RAB comparison of proposed MMA with previously reported studies. It is noted that the proposed MMA shows better RAB of 34% with absorption bandwidth of 1.88 THz (4.57–6.45 THz). In previous studies, the broad-band absorption characteristics are typically demonstrated by incorporating multiple metallic resonators [28, 60] and stacked metallic layers [62, 63] into a single unit cell. In addition, the proposed MMA exhibits higher RAB of 34% with polarization-insensitive characteristics than that of the previously reported single metallic structure-based MMA (17%) [49].

The optimized structure of the proposed MMA, *i.e.*, split-circular ring joined diagonally, along with higher order of resonances from the single metallic structure as shown in Fig. 10a–e, enables the dual multi-and broad-band absorption characteristics which are better than that of the above-mentioned previous studies. In addition, relatively simple design of MMA utilizing continuous single graphene layer makes fabrication easier for practical THz applications unlike graphene hollow petal structure [51].

4 Conclusion

In summary, we have demonstrated a graphene-based metamaterial absorber at terahertz frequencies demonstrating both multi- and broad- band absorption characteristics. Broad-band absorption reaches over 90% for the range of 4.57–6.45 THz with the dual-band absorption peak at 6.86

Table 2 Comparison of the previously reported multi-band MMAs with our proposed MMA

Refs	Technique used	Frequency	Peak numbers	Absorptivity	Polarization	Angles
[54]	Multiple metallic resonators	100–400 THz	4	92.80–99.39%	–	–
[55]	Two metallic resonators	0–4.5 THz	5	98.9–99.8%	–	0–90
[56]	Single metallic resonator	0.5–4 THz	4	75–95%	TE	0–45
[57]	Multiple metallic resonators	60–240 THz	3	97.8–99.5%	–	–
[58]	Multiple metallic resonators	1.5–2.5 THz	2	99.6–99.8%	TE	0–30
[59]	Multiple metallic resonators	0.1–1 THz	5	79.26–99.43%	TM	0–60
				90.44–99.88%	TE	–
Proposed MMA	Single metallic resonator	4–8 THz	5	95.2–99.4%	TM	–
				90–99.7%	TE	0–90

Table 3 Comparison of the previously reported broad-band MMA's RAB with our proposed MMA's RAB

Refs	RAB (%)	Central frequency (THz)	Absorption	Structure
[28]	25.1	4.90	>90%	Four VO$_2$ resonators/polyimide/Au
[60]	20.17	34.20	>80%	Multi-circular gold patches/graphene/polymer/Au
[61]	31.9	3.07	>90%	Au/SiO$_2$ with eight embedded graphene stack columns (graphene sheet and Al$_2$O$_3$)/Si/Au
[62]	31.2, 10.5	1.6, 4.75	>95%	Ion-gel/discrete graphene pattern/dielectric1/dielectric2/dielectric1/metal
[63]	25.3	6.3	>90%	Periodical graphene pattern/double-layer of graphene sheet sandwiched with SiO$_2$ layer/Au
[51]	26.7	3.06	>90%	Connected hollow petal graphene/dielectric/metal
[49]	17	3.8	>90%	Au/SiO$_2$/Au
Proposed MMA	34	5.51	>90%	Au/graphene/SiO$_2$/Au

and 7.20 THz having 98.9 and 95.2% absorption, respectively. Furthermore, there is no obvious difference between transverse magnetic and electric polarized wave due to the symmetrical geometry of proposed structure which also demonstrates polarization insensitivity upto 90° with average absorption of 98.24 and 96.6% for TM and TE polarization, respectively. To understand the phenomena of absorption, we analyzed the surface current and electric field distributions and estimated the normalized impedance with constitutive EM parameters. Consequently, the proposed absorber could be utilized for potential applications including sensing, imaging, and detection.

References

1. D.R. Smith, J.B. Pendry, M.C.K. Wiltshire, Science **305**, 788–792 (2004)
2. T. Ergin, N. Stenger, P. Brenner, J.B. Pendry, M. Wegener, Science **328**, 337–339 (2010)
3. R. Liu, C. Ji, J.J. Mock, J.Y. Chin, T.J. Cui, D.R. Smith, Science **323**, 366–369 (2009)
4. X. Fang, M.L. Tseng, J.Y. Ou, K.F. MacDonald, D.P. Tsai, N.I. Zheludev, Appl. Phys. Lett. **104**, 141102 (2014)
5. D. Wu, N. Fang, C. Sun, X. Zhang, W.J. Padilla, D.N. Basov, D.R. Smith, S. Schultz, Appl. Phys. Lett. **83**, 201–203 (2003)
6. C.M. Watts, D. Shrekenhamer, J. Montoya, G. Lipworth, J. Hunt, T. Sleasman, S. Krishna, D.R. Smith, W.J. Padilla, Nat. Photonics **8**, 605–609 (2014)
7. P. Jain, A. Thourwal, N. Sardana, S. Kumar, N. Gupta, A. K. Singh. Progress in Electromagnetics Research Symposium, 2017
8. J. Hao, L. Zhou, M. Qiu, Phys. Rev. B **83**, 165107 (2011)
9. A. Fang, T. Koschny, M. Wegener, C.M. Soukoulis, Phys. Rev. B Condens. Matter Mater. Phys. **79**, 241104 (2009)
10. J. Zhou, T. Koschny, C.M. Soukoulis, Opt. Express **16**, 11147–11152 (2008)
11. N.I. Landy, S. Sajuyigbe, J.J. Mock, D.R. Smith, W.J. Padilla, Phys. Rev. Lett. **100**, 207402 (2008)
12. X. Ling, Z. Xiao, X. Zheng, J. Mater. Sci.: Mater. Electron. **29**(2), 1497–1503 (2018)
13. X. Zheng, Z. Xiao, X. Ling, J. Mater. Sci.: Mater. Electron. **28**(11), 7739–7744 (2017)
14. X. Liu, T. Tyler, T. Starr, A.F. Starr, N.M. Jokerst, W.J. Padilla, Phys. Rev. Lett. **107**, 045901 (2011)
15. D. Xiao, K. Tao, Q. Wang, Plasmonics **11**, 389–394 (2016)
16. G. Yao, F. Ling, J. Yue, C. Luo, J. Ji, J. Yao. Opt. Express **24**, 1518 (2016)
17. P. Jain, S. Garg, A.K. Singh, S. Bansal, N. Sharma, N. Sardana, S. Kumar, N. Gupta, A.K. Singh. IEEE 13th Nanotechnology Materials and Devices Conference, 2018
18. P. Jain, A.K. Singh, J.K. Pandey, S. Bansal, N. Sardana, S. Kumar, N. Gupta, A.K. Singh. 6th Edition of International Conference on Wireless Networks and Embedded Systems, 2018
19. X. Huang, H. Yang, S. Yu, J. Wang, M. Li, Q. Ye, J. Appl. Phys. **113**, 213516 (2013)
20. J.W. Park, P. Van Tuong, J.Y. Rhee, K.W. Kim, W.H. Jang, E.H. Choi, L.Y. Chen, Y. Lee, Opt. Express **21**, 9691–9702 (2013)
21. F. Ding, Y. Cui, X. Ge, Y. Jin, S. He, Appl. Phys. Lett. **100**, 103506 (2012)
22. J. Grant, Y. Ma, S. Saha, A. Khalid, D.R. Cumming, Opt. Lett. **36**, 3476 (2011)
23. B.X. Wang, X. Zhai, G.Z. Wang, W.Q. Huang, L.L. Wang, IEEE Photonics J. **7**, 1–8 (2015)
24. Y. Ma, Q. Chen, J. Grant, S.C. Saha, A. Khalid, D.R. Cumming, Opt. Lett. **36**, 945–947 (2011)
25. X. Shen, T.J. Cui, J. Zhao, H.F. Ma, W.X. Jiang, H. Li, Opt. Express **19**, 9401 (2011)
26. X. Shen, Y. Yang, Y. Zang, J. Gu, J. Han, W. Zhang, T.J. Cui, Appl. Phys. Lett. **101**, 154102 (2012)
27. Y. Zhao, Q. Huang, H. Cai, X. Lin, Y. Lu, Opt. Commun. **462**, 443–449 (2018)
28. R.N. Dao, X.R. Kong, H.F. Zhang, X.R. Su, Optik **180**, 619–625 (2019)
29. M.P. Ustunsoy, C. Sabah, J. Alloys Compd. **687**, 514–520 (2016)
30. H.F. Zhang, J.X. Liu, J. Yang, H. Zhang, H.M. Li, Results Phys. **11**, 1064–1074 (2018)
31. B.X. Wang, IEEE J. Sel. Top Quantum Electron. **23**, 1–7 (2017)
32. G.D. Wang, M.H. Liu, X.W. Hu, L.H. Kong, L.L. Cheng, Z.Q. Chen, Chin. Phys. B. **23**(1), 017802 (2014)
33. S. Liu, J. Zhuge, S. Ma, H. Chen, D. Bao, Q. He, L. Zhou, T.J. Cui, J. Appl. Phys. **118**(24), 245304 (2015)
34. D. Hu, H. Wang, Z. Tang, X. Zhang, Q. Zhu, Appl. Phys. A **122**(9), 826 (2016)
35. B.X. Wang, G.Z. Wang, T. Sang, J. Phys. D: Appl. Phys. **49**(16), 165307 (2016)
36. H.Y. Meng, L.L. Wang, X. Zhai, G.D. Liu, S.X. Xia, Plasmonics **13**(1), 269–274 (2018)
37. C.M. Watts, X. Liu, W.J. Padilla, Adv. Mater. **24**(23), OP98–OP120 (2012)
38. B.X. Wang, L.L. Wang, G.Z. Wang, W.Q. Huang, X.F. Li, X. Zhai, J. Light. Technol. **32**(6), 1183–1189 (2014)
39. K.S. Novoselov, V.I. Fal, L. Colombo, P.R. Gellert, M.G. Schwab, K. Kim, Nature **490**, 192–200 (2012)
40. C. Song, X. Xia, Z.D. Hu, Y. Liang, J. Wang, Nanoscale Res. Lett. **11**(1), 419 (2016)
41. R. Gao, Z. Xu, C. Ding, L. Wu, J. Yao. Opt. Commun. **356**, 400–404 (2015)
42. Z. Bao, J. Wang, Z.D. Hu, A. Balmakou, S. Khakhomov, Y. Tang, C. Zhang, Opt. express **27**(22), 31435–31445 (2019)
43. Z. Zhai, L. Zhang, X. Li, S. Xiao, Opt. Commun. **431**, 199–202 (2019)
44. J. Wang, C. Song, J. Hang, Z.D. Hu, F. Zhang, Opt. express **25**(20), 23880–23892 (2017)
45. S. Kalraiya, R.K. Chaudhary, M.A. Abdalla, J. Appl. Phys. **125**(13), 134904 (2019)
46. C.L. Holloway, E.F. Kuester, A. Dienstfrey, IEEE Antennas Wirel. Propag. Lett. **10**, 1507–1511 (2011)
47. Z. Yi, L. Liu, L. Wang, C. Cen, X. Chen, Z. Zhou, X. Ye, Y. Yi, Y. Tang, Y. Yi, P. Wu, Results Phys. **13**, 102217 (2019)
48. Z. Yi, H. Lin, G. Niu, X. Chen, Z. Zhou, X. Ye, T. Duan, Y. Yi, Y. Tang, Y. Yi, Results Phys. **13**, 102149 (2019)
49. Y. Zhang, C. Cen, C. Liang, Z. Yi, X. Chen, M. Li, Z. Zhou, Y. Tang, Y. Yi, G. Zhang, Results Phys. **14**, 102422 (2019)
50. D. Yan, J. Li, Laser Phys. **29**(4), 046203 (2019)
51. S. Wu, J.S. Li, Appl. Opt. **58**(11), 3023–3028 (2019)
52. Y. Zhang, C. Cen, C. Liang, Z. Yi, X. Chen, Y. Tang, T. Yi, Y. Yi, W. Luo, S. Xiao, Plasmonics **14**, 1621–1628 (2019)
53. T.B. Zou, F.R. Hu, J. Xiao, L.H. Zhang, F. Liu, T. Chen, J.H. Niu, X.M. Xiong, Acta. Phys. Sin. **63**, 178103 (2014)
54. B. Mulla, C. Sabah, Phys. E Low Dimensional Syst. Nanostruct. **86**, 44–51 (2017)
55. T. Meng, D. Hu, Q. Zhu, Opt. Commun. **415**, 151–155 (2018)

56. S.C. Bakshi, D. Mitra, L. Minz, Plasmonics **13**(6), 1843–1852 (2018)
57. L. Zhao, H. Liu, Z. He, S. Dong, Opt. Express **26**(10), 12838–12851 (2018)
58. M. Janneh, A.D. Marcellis, E. Palange, A.T. Tenggara, D. Byun, Opt. Commun. **416**, 152–159 (2018)
59. Y. He, Q. Wu, S. Yan, Plasmonics. **14**, 1303–1310 (2019)
60. Y. Zhang, Y. Li, Y. Cao, Y. Liu, H. Zhang, Opt. Commun. **382**, 281–287 (2017)
61. Y. Dong, P. Liu, D. Yu, G. Li, L. Yang, IEEE Antennas Wirel. Propag. Lett. **16**, 1115–1118 (2016)
62. N. Hu, F. Wu, L. Bian, H. Liu, P. Liu, Opt. Mater. Express. **8**, 3899–3909 (2018)
63. P. Fu, F. Liu, G.J. Ren, F. Su, D. Li, J.Q. Yao, Opt. Commun. **417**, 62–66 (2018)